

Short-Range Radar Perception in Outdoor Environments

Giulio Reina¹, James Underwood², and Graham Brooker²

¹ Department of Engineering for Innovation, University of Salento, Lecce, Italy
giulio.reina@unisalento.it

² Australian Centre for Field Robotics, University of Sydney, Sydney, Australia
{j.underwood,gbrooker}@acfr.usyd.edu.au

Abstract. For mobile robots operating in outdoor environments, perception is a critical task. Construction, mining, agriculture, and planetary exploration are common examples where the presence of dust, smoke, and rain, and the change in lighting conditions can dramatically degrade conventional vision and laser sensing. Nonetheless, environment perception can still succeed under compromised visibility through the use of a millimeter-wave radar. This paper presents a novel method for scene segmentation using a short-range radar mounted on a ground vehicle. Issues relevant to radar perception in an outdoor environment are described along with field experiments and a quantitative comparison to laser data. The ability to classify the scene and significant improvement in range accuracy are demonstrated showing the utility of millimeter-wave radar as a robotic sensor for persistent and accurate perception in natural scenarios.

1 Introduction

Accurate and robust perception is critical for an autonomous robot to successfully accomplish its tasks in challenging environments. Imaging sensors can provide obstacle avoidance, task-specific target detection and generation of terrain maps for navigation. However, visibility conditions are often poor in field scenarios. Day/night cycles change illumination conditions. Weather phenomena such as fog, rain, snow and hail impede visual perception. Dust clouds rise in excavation sites, agricultural fields, and they are expected during planetary exploration. Smoke also compromises visibility in fire emergencies and disaster sites. While laser scanners and (stereo) cameras are common imaging sensors affected by these conditions [11], radar operates at a wavelength that penetrates dust and other visual obscurants and it can be successfully used as a complementary sensor to conventional range devices. In addition, radar can provide information of distributed and multiple targets that appear in a single observation. However, radar has shortcomings as well, such as large footprint, specular effects, and limited range resolution, all of which may result in poor environment survey or difficulty in interpretation. Typically, radar outputs power-downrange arrays, i.e. a single sensor sweep contains n samples at discrete range increments dR along

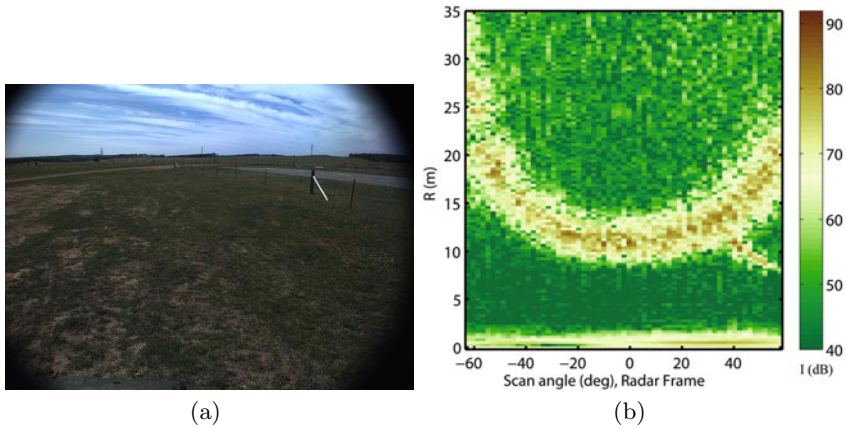


Fig. 1. A sample radar image acquired from a large flat area: camera image approximately colocated with the radar (a), azimuth angle-range image (b)

each azimuth or scan angle. As an example, Fig. 1(b) shows a bidimensional intensity graph of the radar data (radar image) acquired from a large, relatively flat area (Fig. 1(a)). The abscissas in Fig. 1(b) represent the horizontal scanning angle. The ordinates represent the range measured by the sensor. Amplitude values above the noise level suggest the presence of objects with significant reflectivity. Amplitude close or below the noise level generally corresponds to the absence of objects but exceptions exist. These include specular reflecting surface aligned to reflect the signal away, a highly absorbing material, or a total occlusion of radiation. One interesting feature of the radar image is the ground echo, i.e. the intensity return scattered back from the portion of terrain that is illuminated by the sensor beam. In the presence of relatively flat terrain, the ground echo appears as a high-intensity parabolic sector in the radar image (see Fig. 1(b)). This sector is referred to as the radar image background throughout the paper. The ability to automatically identify and extract radar data pertaining to the ground and project them onto the vehicle body frame or navigation frame would result in an enabling technology for all visibility-condition navigation systems. In previous research by the authors, a theoretical model describing the geometric and intensity properties of the ground echo in radar images was described [10]. Here, this model serves as a basis for the development of a novel method for Radar Ground Segmentation (RGS), which allows classification of observed ground returns in three broad categories, namely ground, non-ground, and unknown. The RGS system also improves the accuracy in range estimation of the detected ground for enhanced environment mapping. In addition, non-ground (i.e. obstacles) present in the foreground can also be detected and ranged independently of the ground as high-intensity peaks. Detection and segmentation of ground in a sensor-generated image is a challenging problem with many

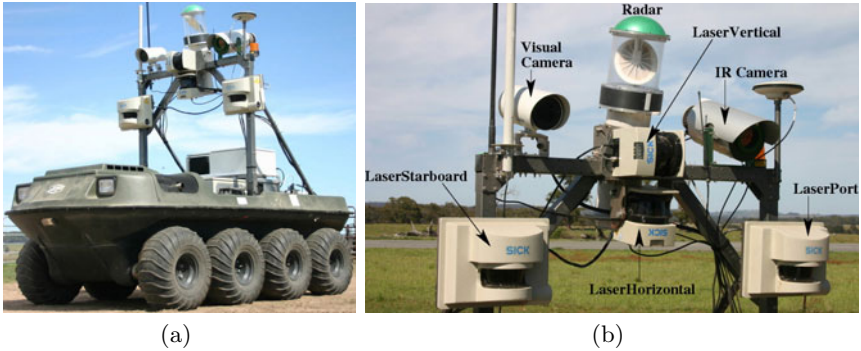


Fig. 2. The CORD UGV employed in this research (a), and its sensor suite (b)

applications in perception. This is a key requirement for scene interpretation, segmentation and classification, and it is important for autonomous navigation [9]. Obstacle detection and avoidance has been commonly performed using ranging sensors such as stereo vision, laser or radar to survey the 3-D shape of the terrain. Some features of the terrain such as slope, roughness, or discontinuities have been then analyzed to segment the traversable regions from the obstacles [7]. In addition, some visual cues such as color, shape and height above the ground have also been employed for segmentation in [3], [6]. Relatively little research has been devoted to investigate millimeter-wave radar for short-range perception and three-dimensional terrain mapping. For example, a millimeter-wave radar-based navigation system detected and matched artificial beacons for localization in a two-dimensional scan [2]. Radar capability was demonstrated in a polar environment [5] and for mining applications [1].

In this investigation, a mechanically scanned millimeter-wave radar is employed. The sensor, custom built at the Australian Center for Field Robotics (ACFR), is a 95-GHz Frequency Modulated Continuous Wave (FMCW) millimeter-wave radar that reports the amplitude of echoes at ranges between 1 and 120 *m*. The wavelength is $\lambda=3\text{mm}$, and the 3 dB beamwidth is about 3.0 deg in elevation and azimuth. The horizontal field of view is 360 deg with an angle scan rate of about 3 *rps*. The range resolution is about 0.32 *m* at 20 *m* [1]. For the extensive testing of the system during its development, we employed the CAS Outdoor Research Demonstrator (CORD) that is an 8 wheel skid-steering all-terrain unmanned ground vehicle (UGV) (see Fig. 2(a)). In Fig. 2(b), the radar is visible, mounted to a frame attached to the vehicle's body and tilted forward so that the center of the beam intersects the ground at a look-ahead distance of about 11.4 *m*. The remainder of this paper is organized as follows. The model of ground echo is recalled in Section 2 and the RGS method is described in detail in Section 3. In Section 4, the RGS system is validated in field tests performed with the CORD UGV. Relevant conclusions are drawn in Section 5.

2 Ground Echo Modeling

For robot perception, an accurate range map of the environment can be obtained from a radar through the scanning of a narrow beam, which is usually referred to as a pencil beam. In the proposed system, the radar is directed at the front of the vehicle with a constant forward pitch to produce a grazing angle β of about 11 deg, as shown in Fig. 3(a). The origin of the beam at the center of the antenna is O. The proximal and distal borders of the footprint area illuminated by the divergence beam are denoted with A and B, respectively. The height of the beam origin with respect to the ground plane is h . The slant range of the radar bore sight is R_0 , the range to the proximal and distal borders is denoted with R_1 and R_2 , respectively. The theoretical model of the ground echo in the radar image was previously developed by the authors. It provides prediction of the range spread of the ground return along with its expected power spectrum. We recall the important properties of the model and refer the reader to [10] for more details. The expected slant distance R_0 can be expressed as a function of the azimuth angle α and the tilt of the robot

$$R_0 = \frac{h}{\cos \theta \cdot \sin \alpha \cdot \sin \phi - \sin \theta \cdot \cos \alpha} \tag{1}$$

where h is the height of the radar from the ground (see Fig. 3(a)), and ϕ and θ are the roll and pitch of the robot, respectively. Similarly, the range of the proximal and distal borders R_1 and R_2 (points A and B in Fig. 3(a)), can be obtained

$$R_1 = \frac{h}{\cos \theta_{el}(\cos \theta \cdot \sin \alpha \cdot \sin \phi - \sin \theta \cdot \cos \alpha) - \cos \theta \cdot \cos \phi \cdot \sin \theta_{el}} \tag{2}$$

$$R_2 = \frac{h}{\cos \theta_{el}(\cos \theta \cdot \sin \alpha \cdot \sin \phi - \sin \theta \cdot \cos \alpha) + \cos \theta \cdot \cos \phi \cdot \sin \theta_{el}} \tag{3}$$

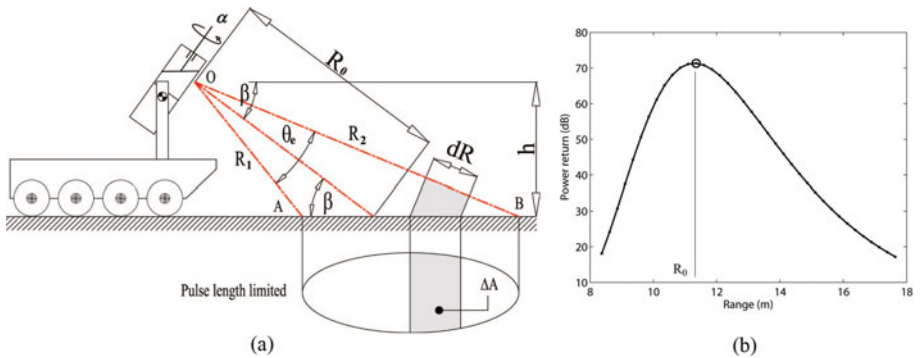


Fig. 3. Scheme of a pencil beam (of beamwidth θ_e) sensing terrain at grazing angle β (a). Simulated power return of the ground echo (b); the following parameters were adopted in the simulation: $k=70dB$, $R_0=11.3m$, $h=2.2m$

Under the assumption that the radar-illuminated ground falls within the so-defined near-field region (i.e. approximately $R < 16m$, [10]), the power return of the ground echo can be expressed as a function of the range R

$$P_r(R, R_0, k) = k \frac{G(R, R_0)^2}{\cos \beta} \quad (4)$$

where k is a constant quantity, G is the antenna gain (usually modeled as gaussian) and β is the grazing angle, as explained in Fig. 3(a). Figure 3(b) shows a simulated wide pulse of the ground return using (4). The model is defined by the two parameters k and R_0 that can be determined in practice by fitting the model to experimental data, as explained later in the paper. In summary, (1) and (4) represent two pieces of information defining the theoretical ground echo in the radar image. Any deviation in the range or intensity shape suggests low likelihood of ground return in a given radar observation.

3 The Radar Ground Segmentation System

A radar image can be thought of as composed of a foreground and a background. The background is referred to as the part of the image containing ground echoes that appear as wide pulses due to the high-incident angle surface. Conversely, obstacles present in the foreground can be detected and ranged as high-intensity narrow pulses. The RGS system aims to assess ground by looking at the image background obtained by a millimeter-wave radar mounted on a mobile robot. It performs two main tasks:

- Background extraction from the radar image.
- Analysis of the power spectrum across the background to perform ground segmentation.

3.1 Background Extraction

Prediction of the range spread of the ground echo as a function of the azimuth angle and the tilt of the vehicle can be obtained using the geometric model presented in Section 2. It should be recalled that the model is based on the assumption of globally flat ground. Therefore, discrepancies in the radar observations may be produced by the presence of local irregularities or obstacles in the radar-illuminated area. In order to relax the assumption of global planarity and compensate for these effects, a change detection algorithm is applied in the vicinity of the model prediction to refine the search. For the mathematical details, we refer the reader to [10], rather than repeating this material here. A typical result is shown in Fig. 4. The radar signal obtained from a single azimuth observation ($\alpha=32\text{deg}$) is denoted by a solid gray line. The theoretical prediction of the range spread of the ground return is shown by black points in the bottom of Fig. 4 representing the range of the central beam, the proximal and distal borders, points R_0 , R_1 and R_2 , respectively. When a positive change in the

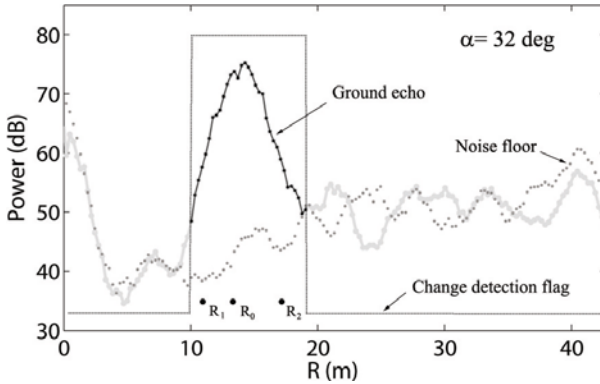


Fig. 4. Ground echo extraction in the radar signal through a change detection approach (a): radar signal at scan angle $\alpha = 32$ deg (gray solid line), extracted ground echo (solid black line), change detection flag (dotted black line). Note that the opposite (i.e. 180-deg scan angle difference) radar signal is also plotted (gray dotted line), it points skyward and no obstacle is detected in it, thus showing the typical noise floor in the radar measurement.

radar signal is found in the vicinity of the proximal border (in practise within a 1-m window centered on R_1), a flag is raised (dotted black line). The alarm is lowered when a negative change is detected in the vicinity of the distal border. The ground echo can, then, be extracted from the given observation (portion of the signal denoted in black). The process can be repeated for the whole scanning range, and the background of the radar image can be successfully extracted.

3.2 Ground Segmentation

The image background contains ground candidates. In order to define a degree of confidence in actual ground echo, the power return model, presented in Section 2, can be fitted to a given radar observation. The hypothesis is that a good match between the parametric model and the data attests to a high likelihood of ground. Conversely, a poor goodness of fit suggests low likelihood due, for example, to the presence of an obstacle or to irregular terrain. We recall that $P_r(R)$, is a function defined by the parameters R_0 and k . k can be interpreted as the power return at the slant range R_0 and both parameters can be estimated by data fitting for the given azimuth angle. By continuously updating the parameters across the image background, the model can be adjusted to local ground roughness and produce a more accurate estimation of R_0 , as shown later in the paper. A non-linear least squares approach using the Gauss-Newton-Marquardt method is adopted for data fitting. The initial parameter estimates are chosen as the maximum measured power value and the predicted range of the central beam as expressed by (1), respectively, limiting the problems of ill conditioning and

divergence. Output from the fitting process are the updated parameters \bar{R}_0 and \bar{k} as well as an estimate of the goodness of fit. The coefficient of efficiency was found to be well suited for this application

$$E = 1 - \frac{\sum(t - y)^2}{\sum(t - \bar{t})^2} \quad (5)$$

t being the data point, \bar{t} the mean of the observations, and y is the output from the regression model. E ranges from $-\infty$ to 1, as the best possible value. By evaluating the coefficient of efficiency and the model parameters, ground segmentation can be effectively performed and radar observations can be labeled as ground, unknown, and non-ground object (i.e. obstacle). Typical results are shown in Fig. 5. Specifically, in Fig. 5(a), the model matches very well the experimental data with a high coefficient of efficiency $E=0.96$, thus attesting to the presence of ground. Conversely, Fig. 5(b) shows an example where the goodness of fit is poor ($E < 0$); in this case a low confidence in ground echo is associated with the given observation. In practice, a threshold Th_E is experimentally determined and the observation i is labeled as ground if E_i exceeds Th_E . However, relying on the coefficient of efficiency, may be misleading in some cases. Figure 5(c) shows an example where a ground patch would be seemingly detected according to the high coefficient of efficiency ($E = 0.91$), when there is actually no ground return. In order to solve this issue, a physical consistency check can be performed by looking at the updated value of the proximal and central range as estimated by the fitting process. For this case, they result almost coincident ($\bar{R}_0=10.82$ m and $\bar{R}_1=10.42$ m, respectively), and certainly not physically consistent with the model described in Section 2. Therefore, the radar observation is labeled as uncertain ground, if the difference between the central and proximal range is lower than an experimentally-defined threshold Th_R . An analogue comparison is done between the distal and central border, as well. In case of uncertain terrain, an additional check is performed to detect possible obstacles present in the region of interest, which would appear as narrow pulses of high intensity. In this respect, it should be noted that, during operation, the RGS system records the value of \bar{k} , defining a variation range for the ground-labeled observation. Typically, \bar{k} was found to range from 73 to 76 dB. If a percentage relative change in the maximum intensity value between the uncertain-labeled observation t_{max} , and the model y_{max} is defined, $\Delta P = \frac{t_{max} - y_{max}}{t_{max}}$, then an obstacle is detected when ΔP exceeds an experimentally defined threshold Th_p and, at the same time, t_{max} is greater than the maximum value of \bar{k} . An example of obstacle (labeled as non-ground) detection is shown in Fig. 5(d). In summary, the classification approach shown in Table 1 can be defined.

4 Experimental Results

In this section, field results are presented to validate our approach for ground segmentation using a millimeter-wave radar. The test field was located in a rural

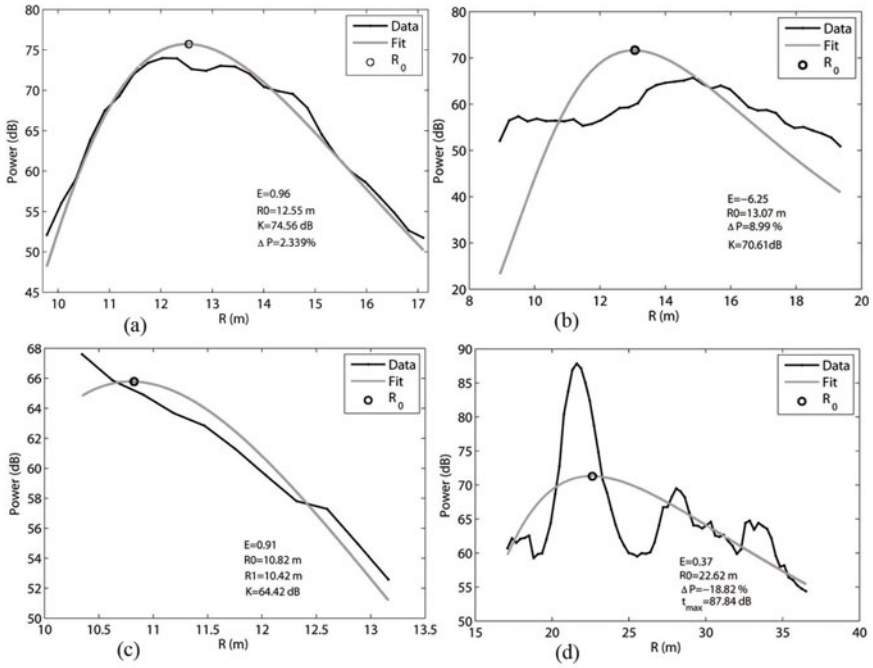


Fig. 5. Ground segmentation by model fitting: good fit labeled as ground (a), poor fit labeled as uncertain ground (b), seemingly high fit labeled as uncertain ground due to physics inconsistency with the model (c), narrow pulse labeled as obstacle (d)

Table 1. Set of rules used by the RGS system for background classification

Class	Goodness of fit ($Th_E=0.8$)	Parameters of the regression model ($Th_R = 1.5m, Th_P = 10\%$)			
	E	$(\bar{R}_0 - \bar{R}_1)$	$(\bar{R}_2 - \bar{R}_0)$	ΔP	k (dB)
Ground	$\geq Th_E$	$> Th_R$	$> Th_R$	$< Th_P$	73–76
Unknown	$< Th_E$	-	-	$< Th_P$	-
Non-ground	$< Th_E$	-	-	$\geq Th_P$	$> k_{max}$

environment at the University of Sydney’s test facility near Marulan, NSW, Australia. It was mainly composed of a relatively flat ground with sparse low grass delimited by fences, a static car, a trailer and a metallic shed, as shown in Fig. 6. During the experiment, the CORD vehicle was remotely controlled to follow an approximately closed-loop path of 210 m with an average travel speed of about 0.5 m/s. In this experiment, the RTK DGPS/INS unit and a high-precision 2D SICK laser range scanner provided the ground truth. The full data set is public and available online [8].



Fig. 6. The Marulan test field is generally flat with a notable exception due to a road running through the side including a significant berm on each edge

4.1 Ground Segmentation and Range Accuracy

Figure 7 shows a typical result obtained during the experiment with a stationary car to the right of the robot. Figure 7(a) shows the radar intensity image overlaid with the results obtained from the RGS system. Ground labels are denoted by black dots, a black cross marks uncertain terrain, and non-ground belonging to the foreground (high-intensity narrow pulses) is denoted by a black triangle. No obstacle belonging to the background is detected in this scan. In Figure 7(b), the results are projected over the image plane of the camera for visualization purposes only. Finally, a comparison with the laser-based ground truth is provided in Figure 7(c), which demonstrates the effectiveness of the proposed approach for ground segmentation. As it can be seen from this figure, the RGS system correctly detected the flat ground area in front of the robot and the obstacle to the right. Uncertain terrain was flagged along the portion of the background occluded by the car and to the far left due to the presence of highly irregular terrain. Overall, the RGS system was tested over 1,100 radar images each containing 63 azimuth observations for a total of 69,300 classifications. As a measure of the segmentation performance, the false positive and false negative rate incurred by the system during classification of ground and non-ground was evaluated by comparison with the ground truth laser data. To this aim, a previously proposed method for segmentation of laser data (GP-INSAC, [4]) was applied to the ground-truth map to extract the true ground and true obstacles. As described in Section 3.2, whenever the RGS system labels data along a particular scan azimuth as ground or non-ground, a range reading is returned. When combined with the localisation estimation of the vehicle, this provides a 3-D georeferenced position for the labeled point. A ground-labeled observation is counted as a false positive if a closest neighbor can not be found in the true ground data within a minimum distance (less than 0.5 *m* in our case). Similarly, a non-ground-labeled point is counted as a false positive if it is not sufficiently close to the nearest true obstacle datum. The rate of false negatives is evaluated by manual inspection in each radar image, instead. The results are collected in Table 2. The percentage of false positives in ground-labeled observations was 2.1%, likely due to seeming matches produced by obstacles present

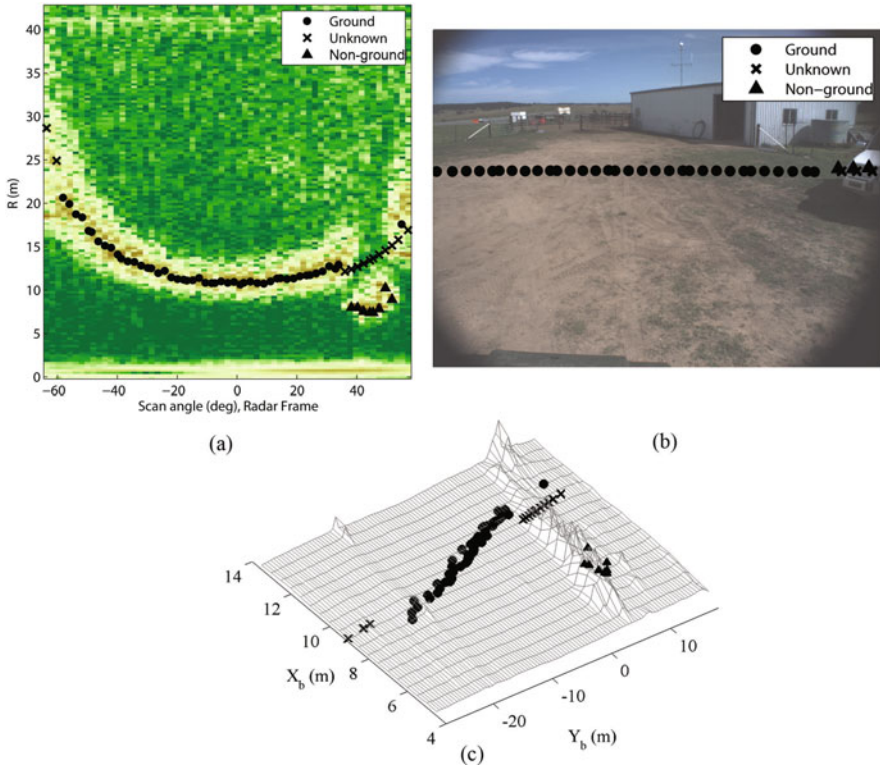
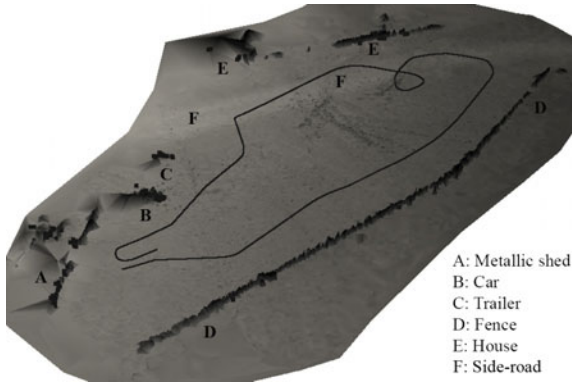


Fig. 7. Output of the RGS system (a), results overlaid over the camera image (b), and over the laser-generated ground-truth map (c)

in the illuminated area. No false positives were detected in the non-ground labeled observations. The false negative rate for the ground-labeled observations was 3.5%. For non-ground-labeled observations, the false negative rate was 5.6%. The average percentage of unknown labels in a single radar image was 19.8%, including occluded areas and false negatives due to radar misreading or low resolution (i.e., footprint overlapping part of an object and ground). It should be noted that false negatives mostly appear in the radar image as spurious observations that do not affect the general understanding of the scene. The accuracy of the RGS system in mapping the ground was assessed through comparison with the true ground map. For the ground-labeled observation i , the RGS system outputs the relative slant range $\bar{R}_{0,i}$. Through geometric transformation, it is possible to estimate the corresponding 3-D point in the world reference frame P_i and to compare it to the closest neighbor of the ground truth map P_i^{gt} . Since the laser-generated map is available as a regularly-sampled grid with square cells of 0.3 m where the center of the grid represents the average height of the cell points, we refer to a mean square error in the elevation E_z . In this experiment, the RGS system detected ground returns in $n = 40150$ observations with an

Table 2. Segmentation results obtained from the RGS system

Class	Observations	False Positives (%)	False Negatives (%)	Accuracy
Ground	40150	2.1	3.5	$E_z=0.051m$
Non-ground	657	0.0	5.6	$E_{xy}=0.065m$

**Fig. 8.** Radar-generated map after Delaunay triangulation

error of $E_z = 0.051m$ and an associated variance of $\sigma_z = 0.002m^2$. If the value of R_0 is measured conventionally taking the intensity peak of the ground return, the error grows to $E_z = 0.251m$ and $\sigma_z = 0.181m^2$. Similarly, the accuracy of the system in measuring the position of detected obstacles can be evaluated by comparison with the nearest datum in the true obstacle map. A mean square error E_{xy} can be defined this time in terms of $x - y$ coordinates. The RGS system measured non-ground returns in $n_1 = 657$ observations with an error of $E_{xy} = 0.065m$ and a variance of $\sigma_{xy} = 0.0015m^2$, thus proving the effectiveness of the proposed approach. For a complete overview of the system performance, the results obtained from the RGS module along the entire experiment are used to build a map of the environment, as shown in Fig. 8 after applying a Delaunay triangulation. The ground labeled-observations are denoted by gray scale dots colored according to the elevation, whereas the obstacle-labeled points are shown by black points for higher contrast. The path followed by the robot is also shown by a solid black line. This figure demonstrates that the RGS system is capable of providing a clear understanding of the environment.

5 Conclusions

In this paper, a novel method for performing ground segmentation was presented using a MMW radar mounted on a off-road vehicle. It was based on the

development of a physical model of the ground echo that was compared against a given radar observation to assess the membership confidence to one of the three broad categories of ground, non-ground, and unknown. In addition, the RGS system provided improved range estimation of the ground-labeled data for more accurate environment mapping, when compared to the standard highest intensity-based approach.

Acknowledgements. The Australian Department of Education, Employment and Workplace Relations is thanked for supporting the project through the 2010 Endeavour Research Fellowship 1745_2010. This research was undertaken through the Centre for Intelligent Mobile Systems (CIMS), and was funded by BAE Systems as part of an ongoing partnership with the University of Sydney. The financial support of the ERA-NET ICT-AGRI is also gratefully acknowledged.

References

1. Brooker, G., Hennessey, R., Bishop, M., Lobsey, C., Durrant-Whyte, H., Birch, D.: High-resolution millimeter-wave radar systems for visualization of unstructured outdoor environments. *Journal of Field Robotics* 23(10), 891–912 (2006)
2. Clark, S., Durrant-Whyte, H.F.: The design of a high performance mmw radar system for autonomous land vehicle navigation. In: *Int. Conf. Field and Service Robotics*, Sydney, Australia, pp. 292–299 (1997)
3. DeSouza, G., Kak, A.: Vision for mobile robot navigation: A survey. *IEEE Transactions on Pattern Analysis and Machine Intelligence* 24(2), 237–267 (2002)
4. Douillard, B., Underwood, J., Kuntz, K., Vlaskine, V., Quadros, A., Morton, P., Frenkel, A.: On the segmentation of 3-d lidar point clouds. In: *IEEE Intl. Conf. on Robotics and Automation*, Shanghai, China (2011)
5. Foessel-Bunting, A., Chheda, S., Apostolopoulos, D.: Short-range millimeter-wave radar perception in a polar environment. In: *International Conference on Field and Service Robotics*, Leuven, Belgium, pp. 133–138 (1999)
6. Jochem, T., Pomerleau, D., Thorpe, C.: Vision-based neural network road and intersection detection and traversal. In: *IEEE/RSJ Intl. Conf. on Intelligent Robots and Systems*, Osaka, Japan (1995)
7. Pagnot, R., Grandjea, P.: Fast cross-country navigation on fair terrains. In: *IEEE Intl. Conf. on Robotics and Automation*, Hiroshima, Japan, pp. 2593–2598 (1995)
8. Peynot, T., Scheduling, S., Terho, S.: The marulan data sets: Multi-sensor perception in a natural environment with challenging conditions. *The International Journal of Robotics Research* 29(13), 1602–1607 (2010)
9. Reina, G., Ishigami, G., Nagatani, K., Yoshida, K.: Odometry correction using visual slip-angle estimation for planetary exploration rovers. *Advanced Robotics* 24(3), 359–385 (2010)
10. Reina, G., Underwood, J., Brooker, G., Durrant-Whyte, H.: Radar-based perception for autonomous outdoor vehicles. *Journal of Field Robotics* 28 (2011)
11. Vandapel, N., Moorehead, S., Whittaker, W., Chatila, R., Murrieta-Cid, R.: Preliminary results on the use of stereo, color cameras and laser sensors in antarctica. In: *Int. Sym. on Experimental Robotics*, Sydney, Australia, pp. 1–6 (1999)